Analysis of the Unsteady Surface Pressure Distribution of a Pitching Airfoil using Modal Decomposition

Pourya Nikoueeyan
University of Wyoming
Jonathan Naughton (naughton@uwyo.edu)
University of Wyoming

Research Article

Keywords: Modal Decomposition, Reduced-order Modeling, Unsteady Pressure Measurement, Dynamic Stall

Posted Date: August 4th, 2022

DOI: https://doi.org/10.21203/rs.3.rs-1910091/v1

Analysis of the Unsteady Surface Pressure Distribution of a Pitching Airfoil using Modal Decomposition

Pourya Nikoueeyan · Jonathan W. Naughton

Received: date / Accepted: date

Abstract This work presents an exploratory attempt to understand how modal decomposition can be utilized for characterizing the behavior of the unsteady surface pressure distribution on a pitching airfoil. The unsteady aerodynamics of a thick airfoil geometry across a wide range of conditions were studied. Analyzing the pressure distributions across cases with different levels of flow separation yielded results that exhibited transitional behavior that encouraged modal analysis. The utility of the Proper Orthogonal Decomposition in capturing the distinct physical features of the unsteady pressure distribution was then evaluated. The first four global spatial modes extracted from surface pressure data resemble important and understandable attributes of the pressure distribution for an oscillating airfoil. The four-mode description sufficiently reconstructs the surface pressure data even for conditions with complex unsteady flow interactions. The resulting reconstructed pressure distributions can be used to approximate lift and moment coefficients with good accuracy.

Keywords Modal Decomposition · Reduced-order Modeling · Unsteady Pressure Measurement · Dynamic Stall

J. W. Naughton
E-mail: naughton@uwyo.edu

University of Wyoming Wind Energy Research Center,
Laramie, WY, USA

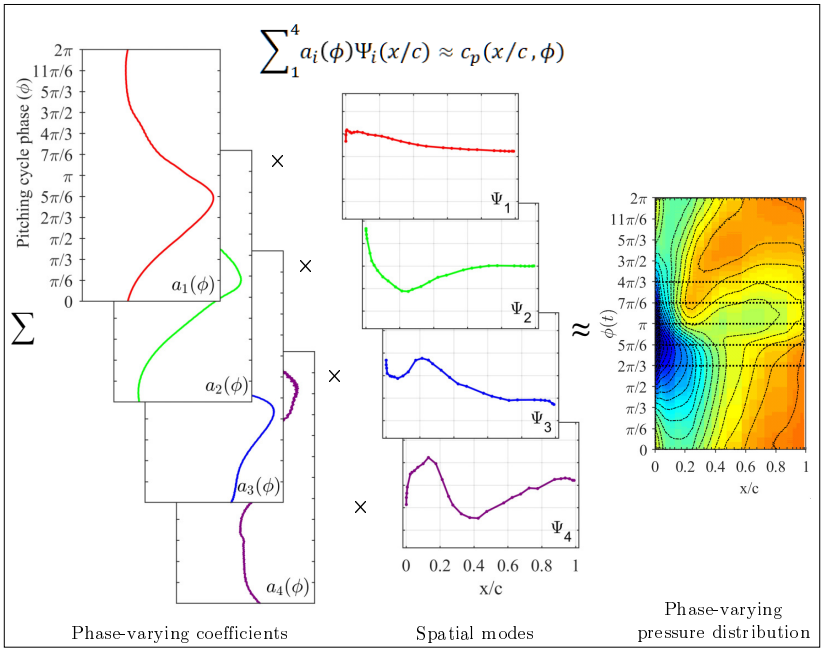

Graphical abstract

1 Introduction

The significance of unsteady flows in today's aerodynamic engineering applications can not be underestimated. Over the past few decades, advancements in experimental and computational fluid dynamics have improved our ability to capture and to understand many unsteady flow phenomena that has resulted in more accurate prediction of unsteady aerodynamics. Along with these improvements, new data analysis techniques such as modal decomposition and reduced-order modeling have also enabled analysis and synthesis of large experimental and computational data sets. These modern approaches have provided initial demonstrations of innovative solutions that can be used to reliably predict the performance of engineering systems under complex unsteady flow conditions.

Modal decomposition is a general term that has been used to refer to a variety of mathematical approaches that aim to provide a simplified description of a random data field using combinations of some deterministic functions. These deterministic functions are often referred to as modes. Unlike Fourier Analysis, modern modal decomposition techniques extract modes from the data field itself (George, 1988). In the discussion of fluid dynamics, the random data field can be the quantity of interest in the flow field under study. Modes in this context are empirical bases that can capture the effect of energetically and dynamically dominant features of the flow field. Taira et al. (2017) and Rowley and Dawson (2017) provide comprehensive reviews of modal decomposition techniques and their application in fluid dynamics. Proper Orthogonal Decomposition (POD), also known as Principal Component Analysis, is a popular modal decomposition technique that is utilized in this investigation. POD was introduced to the fluid dynamics community by Lumley (1967) as a stochastic tool for identifying the energetic coherent structures present in turbulent flows. Over the past two decades, POD has become a mainstream tool for studying unsteady flows. In this context, the main avenues where POD has shown promising prospect are modeling (Walton et al., 2013), flow-state estimation (Durgesh and Naughton, 2010), and active control (Gordeyev and Thomas, 2013).

Among well-known classical unsteady flows, unsteady airfoil aerodynamics has significant practical importance. In the presence of dynamic stall, the nonlinear flow dynamics associated with boundary layer separation, vortex shedding, and flow reattachment can produce complex loading scenarios that are significantly different from quasi-steady approximations. Despite discovering the similarities in the flow structures and many other advancements in characterizing the airfoil behavior in unsteady conditions (McCroskey, 1981; Carr, 1988; Leishman, 2002; Lee and Gerontakos, 2004; Mulleners and Raffel, 2013), accurate prediction and modeling of the unsteady airfoil aerodynamics are still challenges that have not been fully resolved.

Recently, the similarities that exist in the flow structures and the repeatable patterns observed in the surface pressure and flow-field during different stages of dynamic stall have encouraged many to utilize modal decomposition techniques to analyze the unsteady airfoil aerodynamics. In the context of unsteady airfoils, modal analysis has been generally applied to the velocity-field data acquired from Particle Image Velocimetry (PIV) or Computational Fluid Dynamics (CFD) (Mulleners and Raffel, 2012; Mariappan et al., 2014; Dunne and McKeon, 2015; Melius et al., 2016). In contrast, the unsteady surface pressure distribution on moving airfoils have not been widely examined with modal decomposition techniques. Velocity fields are important for providing understanding about the flow structures and as a basis for CFD validation. However, from an experimental perspective, flow-field measurements can be time-consuming to set up, acquire and analyze. By contrast, unsteady surface pressure measurements are typically more straightforward to acquire and analyze, assuming the pressure instrumentation is robust and captures the unsteady attributes of the flow. Calculating aerodynamic forces and moments is also a straightforward processes using surface pressure data. Compared to velocity-field data, pressure distributions are also lower in dimension making modal analysis attractive for real-time state estimation and active flow-control applications.

This study sought to evaluate the efficacy of modal decomposition in the analysis of the unsteady surface pressure measurements acquired on an airfoil over a wide range of unsteady conditions. To achieve this objective, pressure measurements were acquired over a range of angle-of-attack schedules that exhibited a variety of flow conditions. POD was applied to the pressure distributions from different test cases concatenated to form one large data set. The effectiveness of the resulting global modes and their phase-varying coefficients in capturing important features of the unsteady pressure distributions were evaluated. The resulting aerodynamic loads calculated using the reconstructed pressure distributions are used to assess this approach for practical applications. The results indicate that a limited number of global modes are sufficient for characterizing the range of unsteady flows studied here and for providing a low-dimensional estimation of the pressure distributions and loads.

2 Background

Modal analysis has been widely used for the characterization and modeling of unsteady flow problems. Proper Orthogonal Decomposition (POD) and Dynamic Mode Decomposition (DMD) are among the widely utilized modal analysis approaches that have been applied to boundary layers (Bakewell and Lumley, 1967), jets (Citriniti and George, 2000), wakes (Kopp et al., 1997) and cavity flows (Cazemier et al., 1998). Velocity field data, extracted from experiments or computational simulations, have been typically used for data-driven modal analysis of these canonical flows. In these studies, modal analysis provides a means for extracting coherent flow structures and describing their dynamics. Taira et al. (2019) have provided a comprehensive review of recent applications of different modal analysis techniques in characterization, modeling, and control of canonical aerodynamic flows.

Aside from velocity fields, surface-pressure fields have also been widely used for modal characterization of unsteady flows. In this context, the unsteady surface pressure distributions are analyzed to extract the existing features in the pressure field or to shed light on the dynamics of the coherent flow structures via their pressure footprints. The fluctuating pressure distributions on engineering structures, such as storage silos and tanks, have been extensively analyzed using modal decomposition techniques (Tamura et al., 1999; Macdonald et al., 1990). More recently, Gordeyev et al. (2014) studied the unsteady pressure fluctuations around a hemisphere-on-cylinder turret geometry by applying POD on the surface pressure data acquired using Pressure Sensitive Paint (PSP). From a practical standpoint, Ali et al. (2016) have compared the effectiveness of DMD and POD in capturing multi-frequency pressure distributions within an acoustic resonance cavity.

In the arena of unsteady airfoil aerodynamics, the flow field around fixed and dynamically pitching airfoils has been investigated using modal analysis. Glauser et al. (2004) used POD to demonstrate the low dimensionality of the flow field around a fixed angle-of-attack airfoil in pre- and post-stall conditions. From a flow-state-estimation perspective, they also showcased that, by combining POD with Linear Stochastic Estimation, instantaneous pressure measurements on the airfoil surface can be used to obtain time-dependent POD coefficients. Seidel et al. (2005) later showed that a closed-loop flow control scheme can use estimated POD coefficients as the feedback parameter to reattach the separated flow on a stalled airfoil. By utilizing simultaneous time-resolved surface pressure and PIV measurements, Mulleners and Raffel (2012) studied the development of the unsteady flow field within a single dynamic stall life cycle and demonstrated that POD can be effectively used to characterize the onset of dynamic stall. Mariappan et al. (2014) highlighted the differences between POD and DMD in analyzing the flow field around a pitching airfoil undergoing dynamic stall. They showed that, under most measures, POD performs slightly better than DMD; however, they argue that the analytical nature of the DMD makes it more ideal for practical applications.

While the aforementioned body of work has proven that modal analysis is effective in providing a low-dimensional description of the flow field around a pitching airfoil in a variety of conditions, acquisition and processing of the PIV or PSP measurements in investigations with a large number of test cases can be tedious. Additionally, using such techniques in feedback control applications is impractical. Utilizing modal decomposition for analysis of conventional surface-pressure data acquired with pressure taps or surface-mount pressure transducers can provide a more practical approach, especially for determining global modes from a large number of test cases. Coleman et al. (2019) has recently applied a parametric modal decomposition technique to study the dynamic stall phenomenon. Their approach combines pressure difference fields with information about the airfoil's angle of attack schedule to extract modes that are globally optimized across different testing conditions. They have successfully demonstrated the utility of modal decomposition as a reduced-order modeling technique for predicting the aerodynamic loading of an airfoil in complex dynamic stall conditions. However, interpreting the mode shapes and their role in capturing different attributes of the unsteady flow over the airfoil were only briefly considered.

The focus of this paper is to gain a physical understanding of the modal description of unsteady surface pressure distribution. To understand the conditions under which global POD modes and their coefficients reconstruct the unsteady pressure distribution on an airfoil, surface pressure contours are studied in detail as opposed to integrated aerodynamic loads. If modal decomposition can describe the unsteady pressure behavior around an airfoil undergoing dynamic pitching, and if this description can be achieved using a limited number of modes, it is then important to understand the role that these modes are playing in reconstructing the pressure distribution. Understanding the role and relative importance of each mode can help us to predict how time-varying coefficients should behave in different flow regimes. This understanding would allow for a more effective utilization of modal decomposition for flow-state estimation and reduced-order modeling applications.

3 Approach

In this section, the experimental setup is presented along with a short description of the unsteady pressure measurement system. Test cases that were considered are summarized, and a brief mathematical description of the POD method is also provided.

3.1 Experimental Setup

The airfoil to be studied was mounted vertically in the University of Wyoming's low-speed, open-return wind tunnel. The tunnel has a $0.61 \times 0.61 \times 1.22$ m test section and is capable of a range of speeds between 10 to 50 m/s using a variable frequency drive. Free-stream turbulence intensity at 45 m/s is approximately 0.3 percent. A schematic of the test section is shown in Figure 1.

Dynamic pitching of the airfoil was achieved using an in-house designed pitching mechanism that consists of a 24 VDC motor connected to the airfoil through a four-bar linkage. Angular position was recorded through two 13-bit absolute rotary encoders with 0.044 degree resolution connected to the bottom side of the driving mechanism and the top side of the airfoil.

The airfoil section considered for the POD analysis was a flatback version (Barone et al., 2009) of the original Delft University DU97-W-300 airfoil with a trailing edge thickness equal to 10% of the chord length. The instrumented section of the 0.203 m (8 in) chord airfoil was fabricated using stereo-lithography. The section was embedded with 59 pressure taps with a diameter of 0.86mm that were routed to pressure sensing modules through vinyl tubing. The distribution of the pressure taps on the top and bottom surfaces of the airfoil is shown in Figure 2. The airfoil section was tripped near the leading edge to result in a boundary layer behavior similar to that found in higher Reynolds number conditions. Determining the appropriate tripping was accomplished by trying different parameters (location of the trip layer, thickness of the trip layer, and composition) and comparing the resulting pressure profiles with data on the same geometry at a higher Re number reported by Barone et al. (2009). For a detailed description of how the best trip was determined, the reader is encouraged to refer to Nikoueeyan et al. (2014).

3.2 Unsteady Pressure Measurement

Two TE Connectivity (PSI) conventional ESP-32HD pressure scanners each consisting of 32 separate channels were used to capture the unsteady pressure distribution. The pressure scanners used have a static accuracy of ±0.2% Full Scale (FS). The measurable pressure range is ±1 psid. The pressure taps on the airfoil were split between the ESPs such that one ESP read the pressure (bottom) side taps and the other read the suction (top) side taps. The two ESPs were scanned simultaneously at an aggregate sampling frequency of 20 kHz translating to a per-port sampling frequency of 625 Hz.

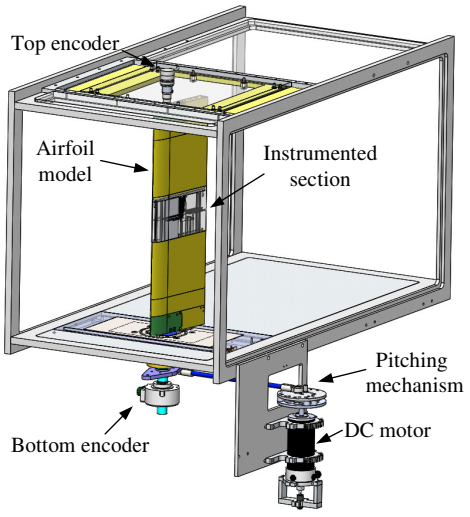

Fig. 1: Schematic of the experimental setup used in this study

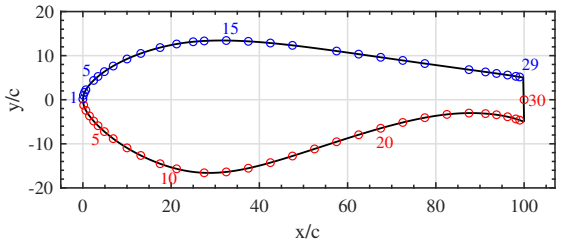

Fig. 2: Airfoil shape under study and the distribution of the pressure taps on the top (blue) and the bottom (red) surfaces

The tubing between surface ports and pressure scanners imposes distortion on the pressure signal. The frequency-dependent amplitude attenuation and phase-lag can be quite significant for the tubing setup described in the previous section. To account for these distorting effects, the Weiner Deconvolution method described by Whitmore and Wilson (2011) was utilized. For reduced frequencies considered in this study, this technique can reconstruct the original pressure signal with good accuracy (Hind et al., 2017). For further information regarding the application of the Weiner Deconvolution in similar wind tunnel testing applications, the reader should refer to Strike et al. (2010) and Nikoueeyan et al. (2019).

To account for the cycle-to-cycle variability and scatter in the unsteady pressure measurements, phase-averaging was performed on the data acquired for each port. Figure 3 demonstrates the scatter of all instantaneous measurements acquired for a single port on the airfoil as a function of phase and angle of attack. The phase-averaged pressure signal is also presented in the same figure. The simultaneous angle-of-attack measurement allows for sorting the pressure data into a pre-specified number of bins N_ϕ. To select an appropriate number of bins, one should consider the resulting number of samples in each bin and the accuracy of the encoder monitoring the angle-of-attack. The former affects the uncertainty of the phase-averaged pressure measurements and should be selected carefully (Lind and Jones, 2016). For the purpose of brevity, the discussion of uncertainty is not presented in this paper, and the reader is referred to Naughton et al. (2013), Davidson et al. (2015) and Hind et al. (2017) for a more detailed description of the analysis of the pressure measurements and the uncertainty analysis as it relates to this study.

3.3 Test Cases

To evaluate the efficacy of the POD technique in the analysis of the unsteady surface pressure measurements, a wide range of pitching conditions are considered that induce different dynamic stall regimes. The instantaneous angle-of-attack schedule $\alpha(t)$ for each test case can be defined by $\alpha(t) = \alpha_0 + \alpha_1 \sin(\omega t)$, where $\omega = 2\pi f$ is the circular frequency. The airfoil was oscillated around its quarter chord axis at two different nominal frequencies. All test cases were performed under conditions of $Re = 4.5 \times 10^5$ and $M_\infty = 0.13$, corresponding to $U_\infty = 45.0$ m/s, and reduced frequencies k ($= \frac{\omega c}{2U_\infty}$) of 0.1 and 0.14 corresponding to oscillation frequencies of 7 Hz and 10 Hz. Table 1 summarizes the parameters for all test cases considered in this study.

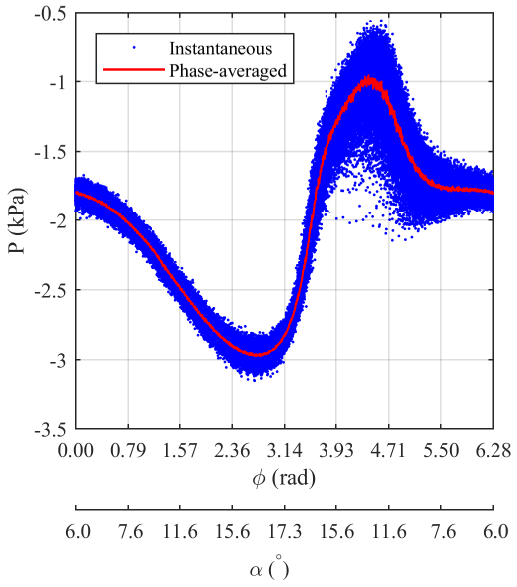

Fig. 3: Instantaneous and phase-averaged pressures plotted against phase, and angle-of-attack from a pressure port located at $x/c = 0.25$ on the top surface of the airfoil (case 11).

Table 1: Pitch oscillation cases used to determine the POD modes.

Case #	α_0	α_1	k	Stall regime
1	7.0	5.7	.14	no stall
2			.10	
3	9.0		.14	
4			.10	
5	9.5		.14	
6			.10	
7	10.2		.14	minor flow reversal
8			.10	stall onset
9	11.1		.14	light stall
10			.10	
11	11.6		.14	moderate stall
12			.10	
13	14.4		.14	
14			.10	
15	15.2		.14	deep stall
16			.10	

3.4 Proper Orthogonal Decomposition

The goal of the Proper Orthogonal Decomposition is to decompose a time-varying field (e.g. pressure or velocity) into a linear combination of basis functions Ψ_k, each multiplied by their corresponding time-varying coefficients $a_k(t)$. In essence, POD provides a means to split the spatial and temporal content of the data (Taira et al., 2017)

$$f(x,t) = \sum_{k=1}^{N} a_k(t)\Psi_k(x). \tag{1}$$

Equation 1 is called the Proper Orthogonal Decomposition of the function $f(x,t)$; $\Psi_k(x)$ are the spatial POD modes and $a_k(t)$ represent the time-varying coefficients associated with each mode. Note that N refers to the number of state variables (e.g. number of velocity probes in a flow or pressure sensors on a surface). The value of $a_k(t)$ conveys the significance of the kth mode at time instance t. Summing over all N modes results in a complete reconstruction of the field, but, a subset of the modes provides a reduced-order approximation that is optimal in a least-square sense. For a detailed discussion about the optimal nature of the POD, the reader is encouraged to consult Holmes et al. (2012) and Buljak (2012). Finding the optimal basis functions can be reduced to the eigenvalue problem (Holmes et al., 2012)

$$R\Psi_k = \lambda_k \Psi_k, \tag{2}$$

where R is the spatial correlation matrix of the pressure measurements. For the details of calculating the correlation matrix R and other instructions on utilizing POD analysis for unsteady surface pressure measurements, refer to Appendix A. Once eigenvectors are determined, time-varying coefficients $a_k(t)$ can be calculated by projecting $f(x,t)$ onto $\Psi_k(x)$ using

$$a_k(t) = (f(x,t), \Psi_k(x)), \tag{3}$$

where $(,)$ represents the inner product.

In this study, the aerodynamic pressure distribution along the chord line is considered in terms of pressure coefficients; as a result, $c_p(x,t)$ is the aerodynamic quantity of interest to be studied using POD. Since unsteady surface pressure measurements on the airfoil surface are usually reported as a function of non-dimensional chord-wise location, x/c is used to denote the spatial distribution of the pressure field. Also, as described earlier, pressure measurements are phase-averaged, and, accordingly, the phase of the airfoil ϕ is used instead of time t for the temporal component in the POD analysis of this work. Equation 1 can be rewriten as

$$c_p(x/c,\phi) = \sum_{k=1}^{N} a_k(\phi)\Psi_k(x/c) \tag{4}$$

to better reflect the POD of the phase-averaged surface pressure coefficients discussed in this study.

4 Results

In the results section, unsteady surface pressure measurements are presented first along with lift and moment coefficients to shed light on the existence and extent of the unsteady flow features. Then, results from POD analysis are presented by discussing how each mode contributes in reconstructing the pressure distribution under different stages of dynamic stall. At the end, the effectiveness of modal description will be assessed in approximating aerodynamic loads from a reduced-order modeling stand point.

4.1 Unsteady surface pressure distributions and loads

Prior to the modal analysis of the unsteady surface pressure distribution to be discussed in the next section, it is beneficial to assess the breadth of unsteady conditions experienced by the airfoil across different testing conditions summarized in Table 1. Note that the phase-averaged analysis of the surface pressure distribution provides valuable insight into the typical behavior of the unsteady airfoil aerodynamics and are considered in this study. A similar analysis could be applied to instantaneous results but is beyond the scope of this paper. For a detailed analysis of the cycle-to-cycle variation of the dynamic stall process and instantaneous pressure measurements, the reader is encouraged to consult Ramasamy et al. (2018) and Harms et al. (2018).

The range of conditions considered in this work resulted in very different dynamic stall behaviors. Five different cases from Table 1 are highlighted in Figure 4 to showcase this wide range of dynamic stall

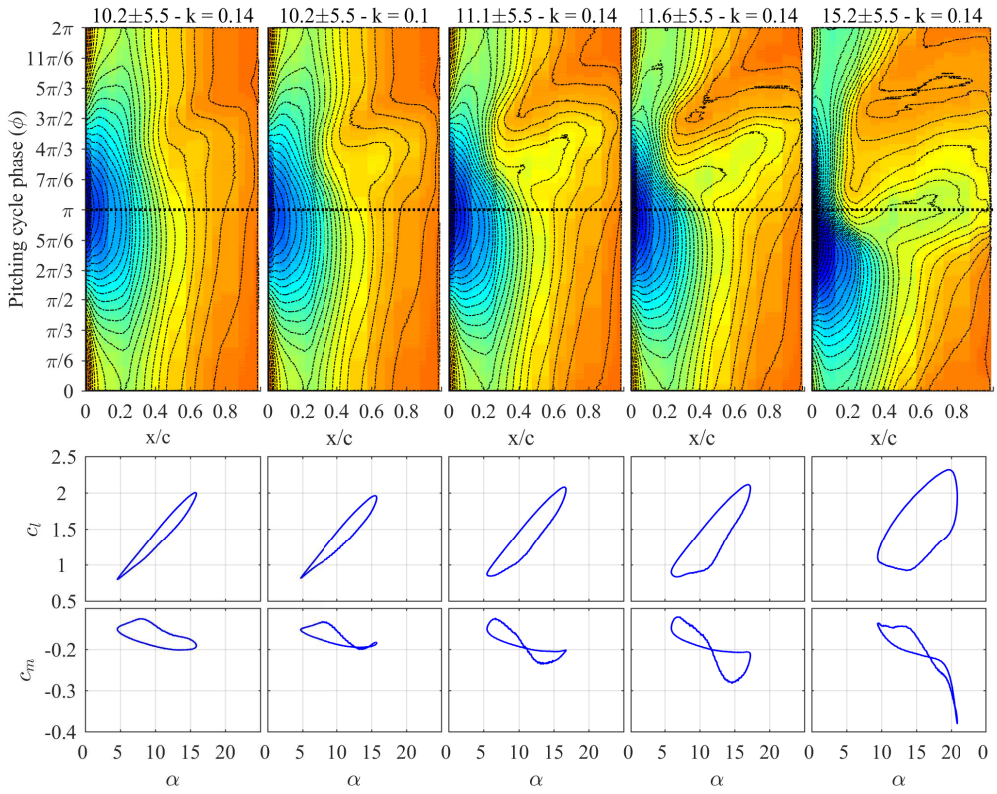

Fig. 4: Phase-averaged pressure distributions (top) on the top side of the airfoil and associated lift and moment coefficients (directly below pressure distribution).

behaviors. For each case (columns in Figure 4), the phase-averaged c_p distribution for the top surface (first row) is shown along with the lift (second row) and the moment (third row) coefficients. A detailed description of how to read and interpret the contour representation of c_p data is provided in Appendix B. Note that, unlike Figure 13 in Appendix B, the angle of attack is not shown for the unsteady surface pressure data shown in Figure 4 since the mean angle of attack α_0 is different for each case (except for the first two cases). The amplitude of the oscillations α_1 stays the same in all cases. It should also be noted that, despite the importance of the pressure distribution on the bottom surface of the airfoil, only the phase-averaged pressure distribution of the top surface will be discussed hereafter due to the richness of the unsteady flow behavior on the top surface and for the sake of brevity.

The first case ($\alpha = 10.2^\circ \pm 5.7^\circ - k = 0.14$) represents a condition where flow remains attached to the top surface of the airfoil during the larger part of the cycle. Examining the pressure distribution contours for this case indicates the occurrence of a disturbance in the suction around the mid-chord slightly after airfoil reaches its maximum angle of attack ($\phi > \pi$). This signature is consistent with the effect associated with the formation of a thin low-momentum region near the trailing edge (McCroskey, 1981). As a result of recovering pressure gradient during the falling phase, the effects on the airfoil lift and moment coefficients remain small.

For the same α schedule but lower reduced frequency, the second case ($\alpha = 10.2^\circ \pm 5.7^\circ - k = 0.1$) demonstrates a rather interesting observation about the importance of the reduced frequency. Similar to the first case, a disturbance appears in the pressure distribution during the falling motion with a stronger footprint. The high suction region near the quarter-chord shrinks slightly more than the first case, and the elevation in the suction near the trailing edge is more defined for the second case. These changes in the pressure distribution suggest the occurrence of a weak shear layer roll-up (McCroskey, 1977; Ericsson and Reding, 1988). This observation indicates that the nominal maximum angle of attack α_{max} for the first two cases is sufficiently high to cause stall onset given a sufficiently low reduced frequency (Leishman, 2002). Note that, beyond the maximum incidence angle associated with this case ($\alpha_{max} = 15.9^\circ$), any additional gain in the lift coefficient during the rising phase is accompanied with significant increase in the nose-down pitching moment, a criteria that is typically used to characterize the onset of dynamic stall (McCroskey, 1977).

By further increasing the mean angle of attack to $\alpha_0 = 11.1^\circ$, case 3 in Figure 4, loss of suction in the pressure distribution becomes noticeable. Clearly, the adverse pressure gradient on the top surface

of the airfoil has reached a critical point. The reduction in the region where high suction occurs near the leading edge indicates the separation of the shear layer is in progress between $\phi = 7\pi/6$ and $\phi = 3\pi/2$. Shear layer separation is accompanied with the formation and shedding of the vortical structures that gives rise to the suction near the trailing edge (Ericsson and Reding, 1988; Widmann and Tropea, 2017). The increased suction pressure on the aft portion of the airfoil for the last 3 cases shown in Figure 4 show this phenomenon. This effect on the pressure distribution of the trailing edge is now strong enough to significantly affect the nose-down pitching moment.

For the other cases shown in Figure 4, cases 4 and 5, a further increase in α_0 results in more severe adverse pressure gradients and consequently stronger roll up of the shear layer with clearly defined pressure footprints. The loss of suction in the pressure distributions near the leading edge indicates that the chord-wise extent of the separation continues to grow toward the leading edge and that the flow remains separated for longer periods during each cycle. Additionally, comparing the pressure data for all 5 cases shown in Figure 4 indicates that the timing of the separation process advances in phase reaching the rising portion of the cycle for the highest angle of attack case. These effects result in more severe instances of dynamic stall and create more complex and extreme loading conditions with higher maximum c_l values and much lower c_m values as shown in Figure 4.

The important takeaway from the analysis of the surface pressure data is that the main flow features associated with dynamic stall are present in the cases shown in Figure 4. The differences arise from the timing and strength of the flow features as a function of the airfoil's motion characteristics. The well behaved evolution of the flow and the associated unsteady surface pressure footprints encourage the utilization of modal analysis to further investigate this analogous behavior.

4.2 Modal analysis

The objective of this section is to show the effectiveness of modal analysis in capturing different attributes of the unsteady surface pressure distribution across a wide range of conditions. For brevity, the discussion is narrowed to the top surface of the airfoil.

4.2.1 Modal description of the Aerodynamic behavior for a single case

Even though it is possible to consider each test case independently and to extract a new set of modes for each case, it is preferable to extract a general set of modes and to track their behavior across a range of unsteady flow conditions. This approach allows for a deeper understanding of the modes and their role in reconstructing the surface pressure distribution as flow conditions change. As described in Appendix A, phase-averaged pressure distributions from different cases are concatenated to form a comprehensive data matrix. Solving the eigenvalue problem, described by equation 2, results in a set of 29 spatial modes (equal to number of pressure taps on the top surface) that will be referred to as global modes. The first four dominant modes are shown in Figure 5.

A number of useful observations can be made by examining the mode shapes. The first global mode $\Psi_1(x/c)$ resembles a typical pressure distribution associated with a fully attached flow state. The second mode $\Psi_2(x/c)$ influences the first half of the chord without any significant contribution to the trailing edge area as its magnitude approaches zero past $x/c = 0.6$. The third spatial mode $\Psi_3(x/c)$ can significantly influence the reconstruction of pressure fluctuations near the quarter chord and, importantly, the trailing edge region. The fourth spatial mode $\Psi_4(x/c)$ has a more complex shape compared to the first three modes, and, even though it has a smaller overall effect on the pressure distribution than the first three modes, its shape impacts the entire chord-wise pressure distribution.

To further investigate the modes and their role in approximating the surface pressure distribution, it is important to consider the phase-dependent coefficients $a_k(\phi)$. Figure 6 demonstrates how modes and

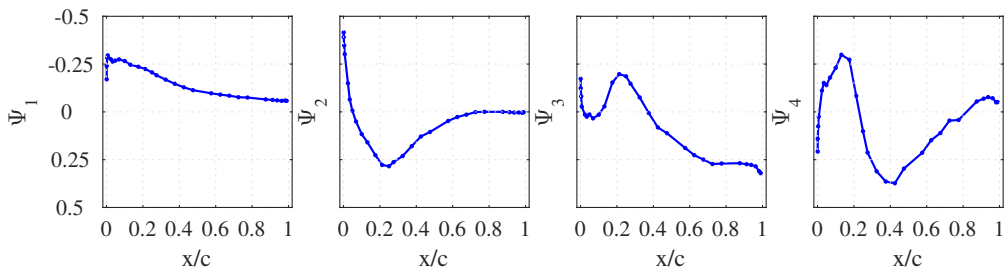

Fig. 5: First four global POD modes associated with the pressure distribution of the airfoil's top surface.

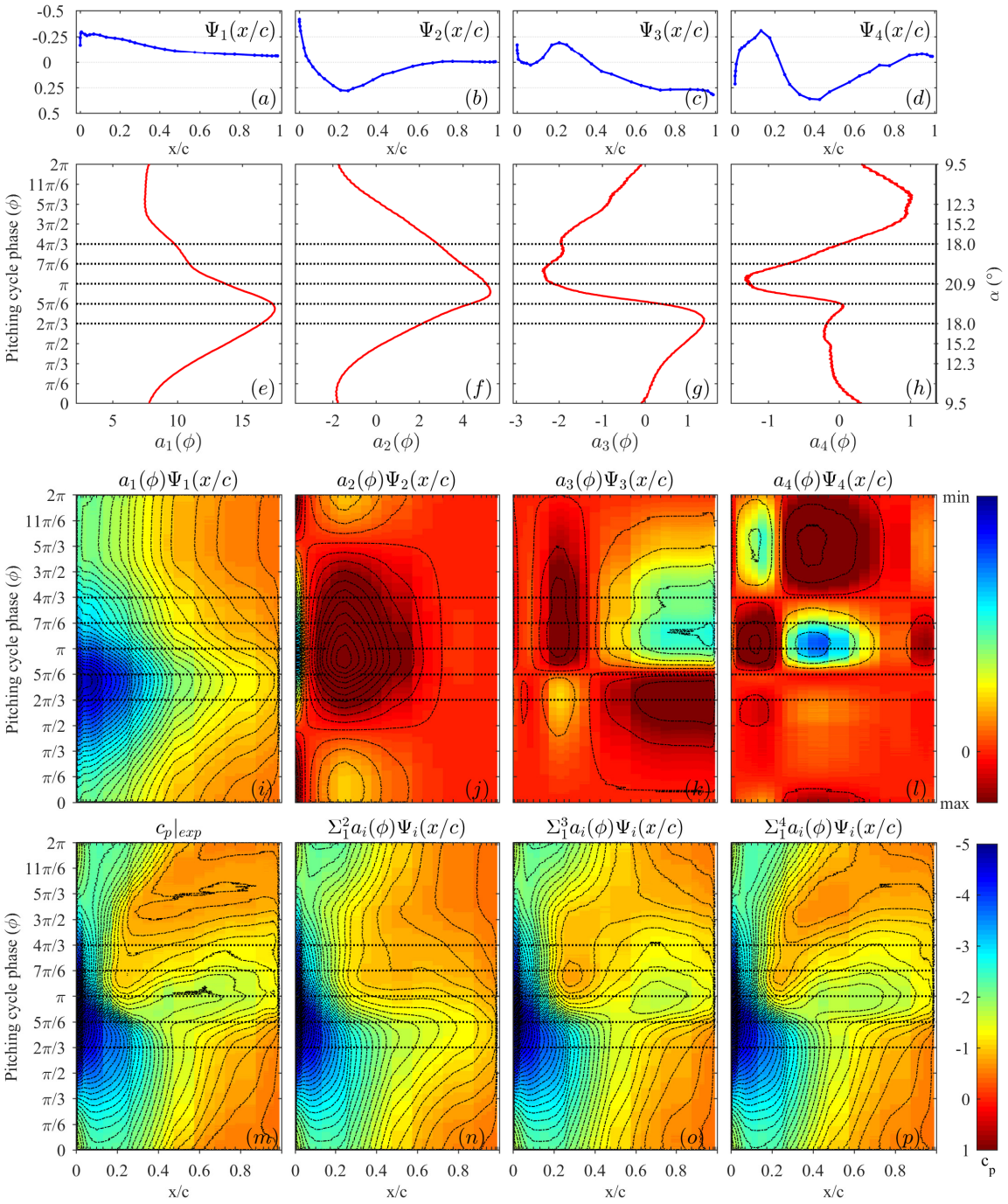

Fig. 6: Modes and their phase-varying coefficients are used to reconstruct the phase-averaged pressure data for case 15: (a-d) The first four global modes, $\Psi_{1-4}(x/c)$; (e-h) phase-varying coefficients associated with the first four modes; (i-l) single-mode reconstructions; (m) the actual pressure distribution; (n-p) reduced-order reconstructions of the pressure distribution.

their phase-varying coefficients reconstruct the phase-averaged pressure data. The top row in Figure 6 repeats the global modes depicted in Figure 5 for convenience. Projecting the phase-averaged pressure distribution of the top surface for any of the test cases discussed earlier onto each one of these modes results in the phase-varying coefficient associated with that mode and specific test case. Here, a deep stall case that was considered previously is examined. For this case, the first four phase-varying coefficients $a_{1-4}(\phi)$ are shown in Figure 6 e-h. To facilitate the comparison with pressure contours, the phase is shown on the vertical axis, and the magnitude of the modal coefficients is shown on the horizontal axis. Note that the modes are orthonormal spatial vectors, and their relative magnitude at each instance in phase is conveyed by the value of their coefficient. It was mentioned earlier that POD modes are

naturally ordered according to their significance, and, as a result, the root mean square (rms) of the phase-varying coefficients drops for higher-order modes as they have a lower impact on the pressure distribution magnitude and capture smaller fractions of the total pressure distribution content. Examining the magnitude of the POD coefficients, $a_{1-4}(\phi)$, validates this property of the modes. Multiplying each mode by its phase-varying coefficient results in single-mode reconstructions of the surface pressure data, which are shown in Figure 6 i-l. In order to highlight the important features, the color bar and associated iso-contour lines for each plot are adjusted based on the minimum and maximum values of each single-mode reconstruction. The summation of the single-mode reconstructions allows for a reduced order representation of the surface pressure data. These multi-mode approximations are shown in Figure 6 n-p. To allow for easier comparison with the actual c_p data, Figure 6 m presents the actual surface pressure distribution for this case.

In the discussion of Figure 5, it was mentioned that the first mode mainly represents the pressure distribution associated with attached flow and does not capture the attributes of separation. Conceivably, the attached flow state is present at least partially during every cycle in all considered cases. As a result, this mode is the most dominant POD mode in all cases. Examining $a_1(\phi)\Psi_1(x/c)$ in Figure 6 i confirms that $\Psi_1(x/c)$ does not capture the pressure changes associated with flow separation. It is also interesting to note that, at the beginning of the cycle, $a_1(\phi)$ varies with phase angle, but, at lower angles of attack toward the end of the cycle, it stays somewhat constant and relies on the higher order modes to recover the more complex features of the pressure recovery during the reattachment process.

The second mode consists of two peaks with opposite signs in the first half of the chord and a flat tail extending to the trailing edge. The first peak is sharper and is located close to the leading edge. The second peak is centered around the quarter chord; it is broader and covers a large extent of the top surface. During a cycle, $a_2(\phi)$ initially takes on negative values to capture a wide suction peak around the quarter chord and lower suction levels near the leading edge, which are the attributes of the pressure distribution for a thick and rounded-nose airfoil geometry at low angles of attack. As angle of attack increases, $a_2(\phi)$ takes on positive values to better reconstruct the leading-edge suction peak that forms due to the increased acceleration of the flow required by the higher angles of attack. The second peak, however, regulates the high suction created by the first mode, especially during the down-stroke motion. As a result, the combination of the first two modes can effectively capture the important changes in the c_p distribution on the front half of the airfoil as seen in the summation of the contributions from modes 1 and 2 in Figure 6 n. It is apparent from Figure 6 j and n that the second mode's role is important at both higher and lower angles of attack. Despite its importance, the second mode has almost no role in capturing the pressure fluctuations near the trailing edge before and after the separation.

Before addressing modes 3 and 4 that influence the c_p distribution near the trailing edge, it is useful to consider the loading curves that can be calculated using the reconstructed c_p distributions. Plotted as a function of phase angle (y-axis), Figure 7 presents c_l and c_m calculated from the c_p reconstructions shown in Figure 6. The number of modes used to reconstruct the c_p distributions increases from left to right. For simplicity, the actual c_p data for the bottom surface of the airfoil are used in aerodynamic load calculations. This allows for isolating the effect of top surface modes that enables a better understanding of the role each mode plays in capturing different attributes of the unsteady surface pressure distribution. Clearly, approximating c_p using only one mode overpredicts the c_l at high angles of attack. However, the addition of the second mode improves the c_l approximation (see Figure 7 b) especially at the beginning and the end of the cycle where trailing edge separation is negligible. On the contrary, the c_m values calculated using the first two modes carry significant error arising from the lack of accuracy in the approximation of the c_p distribution near the trailing edge. Note that the weighting from the distance between rear of the airfoil and quarter chord enhances the impact of the trailing edge c_p distribution on c_m. Consequently, without capturing the c_p distribution near the trailing edge that is significantly affected by the flow separation, c_m cannot be calculated correctly.

As the discussion so far has indicated, the c_p reconstruction based on the first two dominant modes does not resolve the separation-induced pressure distribution on the trailing edge. This is further emphasized by comparing the experimental and two-mode reconstruction results shown in Figure 6 m and n. As previously indicated in the discussion of the third mode shape, its finite magnitude near the trailing edge enables $\Psi_3(x/c)$ to significantly affect the surface pressure approximations on the rear half of the airfoil. In addition to its impact near the trailing edge, third mode also exhibits a peak around the quarter chord area. In contrast to the first mode, modes 2-4 all have a peak that partially covers the quarter chord area. This is a particularly important area on the airfoil during both separation and reattachment processes, and, as a result, the modal description of the pressure distribution requires more degrees of freedom to fully capture the pressure changes in the region around this location. Accordingly, the summation of the first three modes captures, to a fairly good degree, the pressure distribution in both attached and stalled flow as shown in Figure 6 o. The improvement in the pressure distribution is further indicated by the

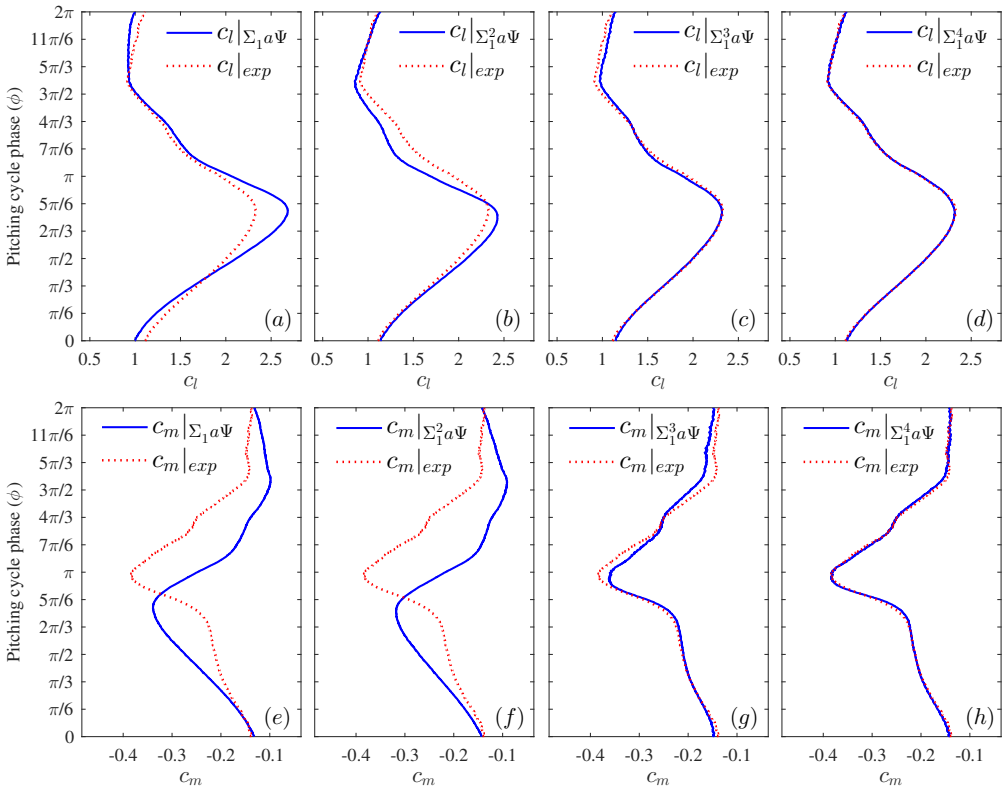

Fig. 7: Lift c_l, and moment c_m, coefficients calculated based on the modal reconstructions for Case 15 are plotted as blue solid lines. The red dotted lines present the lift and moment coefficients calculated using the experimental c_p distribution and are repeated for convenient comparison.

improvements in c_l and c_m curves shown in Figure 7 c and g. Although improved, there is still a slight difference between 3-mode reconstructed c_l and c_m and the experimental results.

Even though the fourth mode has less significance compared to the first 3 modes, the timing of the changes in $a_4(\phi)$ suggests that, similar to the third mode, $\Psi_4(x/c)$ also plays a role during the separation and reattachment processes. The location of the peaks and valleys approximated by a single mode shape are stationary in the spatial direction as phase angle varies. As discussed by Durgesh and Naughton (2010), with real-valued POD modes, traveling structures cannot be reconstructed using single modes, and multiple modes are needed to capture the effect of such features. The complexity of the shear-layer separation process requires multiple modes to capture it's impact on the pressure distribution. By adding the contribution of the fourth mode to the c_p reconstructions shown in Figure 6, the lift and moment coefficients can now be accurately calculated as indicated in Figure 7. It will be discussed later in text that the same number of modes for the bottom surface of the airfoil are sufficient to reach the same level of accuracy in predicting lift and moment coefficients in all stall regimes. This is an encouraging result that corroborates the conclusions made by Coleman et al. (2019) on the effectiveness of modal decomposition in dynamic stall modeling.

4.2.2 Comparison of the modal behavior across different cases

Before examining the trends in the behavior of the phase-varying coefficients under complex stalled conditions, it is useful to examine how they behave under attached flow conditions. Phase varying coefficients are shown for four cases in Figure 8. The angle of attack schedules for cases 1 and 2 are slightly above the static stall angle and do not induce stalled conditions. Cases 5 and 6 have slightly higher mean angle of attack α_0 and demonstrate some small disturbances in the pressure distributions that are due to the growth of the shear layer on the trailing edge (McCroskey, 1981), but the surface pressure contours indicate fast recovery and reattachment. For the no-stall cases, cases 1 and 2, the first 3 modes exhibit a fairly symmetric behavior before and after reaching the maximum angle of attack ($\phi = \pi$) as shown in Figure 8. In the no-stall condition, $a_4(\phi)$ remains fairly small throughout the cycle. For test cases with higher α_0, e.g. cases 5 and 6, the amplitude of $a_1(\phi)$ increases to compensate for the higher suction experienced on the top surface of the airfoil due to the increase in angle of attack. As α increases during the first half of the cycle, the suction peak moves toward the leading edge. As a result,

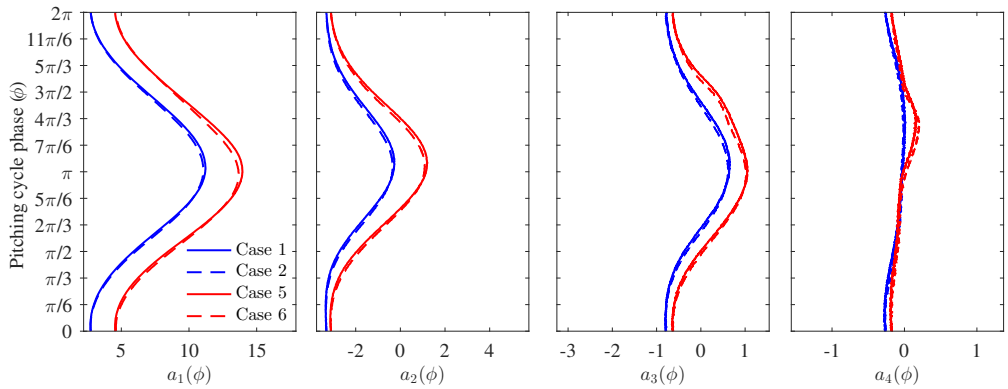

Fig. 8: Phase-varying coefficients for test cases without dynamic stall.

$a_2(\phi)$ reaches positive values around mid cycle to capture the leading edge suction peak. The disturbance that appeared in the c_p distribution of the airfoil during the falling phase in case 7 shown in Figure 4 is also observed in the pressure distributions of cases 5 and 6. As discussed earlier, this feature in the pressure distribution is consistent with the effect that the growth of a thin reversed flow region would induce on the pressure distribution near the trailing edge (McCroskey, 1977; McAlister et al., 1978; Ericsson and Reding, 1988), and it is captured by the third and fourth modes. Compared to cases 1 and 2, the $a_3(\phi)$ curves exhibit a slight increase in their amplitudes while maintaining their shapes for cases 5 and 6. Additionally, as the airfoil begins its falling motion ($\phi > \pi$), a small bump appears in the $a_3(\phi)$ curves that was nonexistent for the no-stall cases. An even more obvious bump appears in the $a_4(\phi)$ curves at similar phase angles. The timing of these two features is aligned with the growth and decline of the aforementioned disturbance in the pressure distribution on the airfoil. This is another example of the interconnection between modes 3 and 4 in reconstructing the effects on pressure distribution associated with flow separation and reattachment. It is also important to note the insignificant effect of reduced frequency on the phase-varying coefficients for cases shown in Figure 8. This behavior is expected for the unsteady flow around pitching airfoils with $\alpha_{max} < \alpha_{ss}$. Generally, at lower angles of attack, the flow does not exhibit significant dependency on the reduced frequency (McAlister et al., 1978).

In the analysis of the phase-varying coefficients, an important case for consideration is the onset of dynamic stall. Figure 9 exhibits the phase-varying coefficients $a_k(\phi)$ associated with the first four global modes for cases 7 and 8. Phase-varying coefficients for the first two modes do not exhibit significant difference for the two reduced frequencies shown in this figure. However, it is important to point out that $a_1(\phi)$ for case 8 has slightly lower values during the falling phase. It was shown earlier in Figure 4 that, for the lower reduced-frequency of case 8, the rise in the c_p distribution on the mid-chord and aft region of the airfoil implies a stronger case of flow separation during the falling phase of the cycle compared to case 7 with the higher reduced-frequency. As a result, the chord-wise suction distribution that is mainly captured by the first mode shape becomes less significant during the falling motion, and, consequently, $a_1(\phi)$ for case 8 has slightly lower values compared to case 7. Comparing $a_3(\phi)$ and

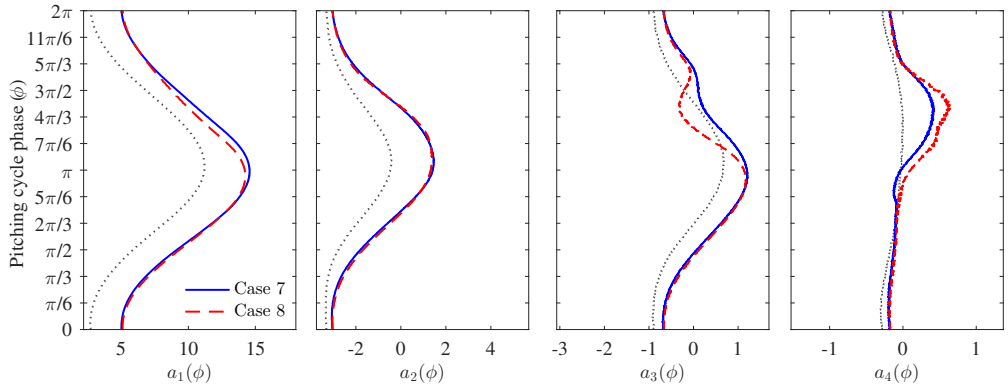

Fig. 9: Phase-varying coefficients for test cases 7 and 8 pertaining to the onset of dynamic stall. The phase-varying coefficients for case 1, the case without dynamic stall, are shown with dotted lines for reference.

$a_4(\phi)$ shown in Figure 9 to their counterparts for case 5 and 6 in Figure 8, it is clear that, as stall develops, the phase-varying coefficients for mode 3 and 4 change significantly. For the two reduced frequencies presented in Figure 9, $a_3(\phi)$ and $a_4(\phi)$ show significant frequency dependence during the separation/reattachment process; unlike previous cases (e.g. case 5 and 6) that exhibited negligible dependence during the entire cycle. It was discussed earlier that, due to a lower reduced frequency, the stronger pressure disturbance near the trailing edge for case 8 indicates a more severe case of separation compared to case 7. Accordingly, $a_3(\phi)$ and $a_4(\phi)$ increase more rapidly for case 8, compared to case 7, to capture the more significant pressure changes.

From Figures 8 and 9, it appears that the behavior of the phase-varying coefficients follows observable trends. To further illustrate such trends, Figure 10 is presented. The modal coefficients associated with the first four global modes are shown for 5 different cases as functions of phase angle. All five cases have the same reduced frequency, $k = 0.14$ to isolate the angle-of-attack effects. The phase-varying coefficients for the attached flow case (lowest α_0) is plotted in dark blue, and that of the deepest stall case (highest α_0) is plotted in dark red with the cases in between colored according to their α_0. A trend that can be observed in the behavior of all phase-varying coefficients is the loss of symmetry across the mid-cycle point ($\phi = \pi$) for deeper stall cases. As α_{max} increases, more severe instances of dynamic stall take place. Consequently, the phase-varying coefficients lose their symmetry across the mid cycle point, and modes 3 and 4 start to play a more important role in capturing the associated pressure fluctuations. Another clear trend that can be observed for the first 3 modal coefficients is that, in the first part of the cycle prior to separation, the magnitude of the phase-varying coefficients increases as α_0 increases. The behavior of $a_3(\phi)$ and $a_4(\phi)$ curves during stall is of particular interest. For $a_3(\phi)$, the advancement of the location of its peak value in phase and sharper fall in its values followed by slower recovery during the falling phase of the cycle capture the behavior of the shear layer and its effect on the pressure distribution during the stall process. The $a_4(\phi)$ values seem to stay close to zero during the attached part of the cycle for all 5 cases shown in Figure 10. As separation takes place, $a_4(\phi)$ takes on larger magnitudes as the strength of the stall increases. Note that $a_4(\phi)$ for case 13 does not return to its pre-stall magnitudes until the rising phase of the cycle, since the flow reattaches during the rising portion of the cycle.

To further consider the role of each mode under different conditions, it is useful to consider the eigenvalues associated with the four dominant modes and to examine the changes in the eigenvalues across the parameter space considered in this work. The eigenvalue of each mode λ_k is the mean square value of the $a_k(\phi)$ (Alfonsi et al., 2001) calculated after projecting the pressure data onto global modes. Figure 11 is used to compare the eigenvalues associated with the first four global modes for test cases summarized in Table 1. The mean angle of attack α_0 for each testing case is shown on the horizontal axis. In each subfigure, the eigenvalues are shown on the left vertical axis (in red), while their relative contributions to the total modal energy are shown on the right vertical axis (in blue).

Examining the behavior of the absolute eigenvalues also supports different observations that have been reported throughout this paper. As expected, the absolute value of the first eigenvalue continues to increase to account for higher suction pressure experienced for cases with higher α_0. However, at higher angles of attack, the complexity of the pressure distribution associated with flow separation requires higher order modes, and, as a result, the relative contribution of the first mode plateaus around stall onset and declines thereafter. The eigenvalue of the second mode is high at lower angles of attack. Note that, at these lower α_0 values, the phase varying coefficient is negative to suppress the suction at the leading edge and to help with the broader suction distribution around the quarter chord. As α_0 increases for subsequent cases, the contribution of $a_2(\phi)$ should increase in the positive direction to account for

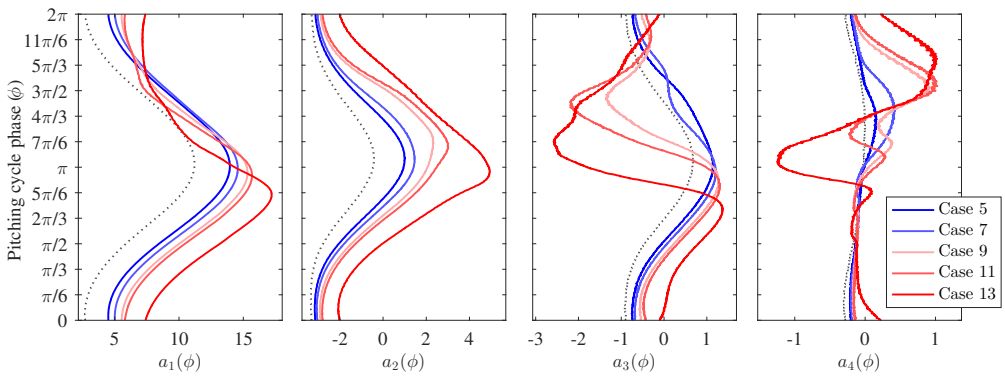

Fig. 10: Phase-varying coefficients for selected cases with $k = 0.14$. The phase-varying coefficients for case 1, the case without dynamic stall, are shown with dotted lines for reference.

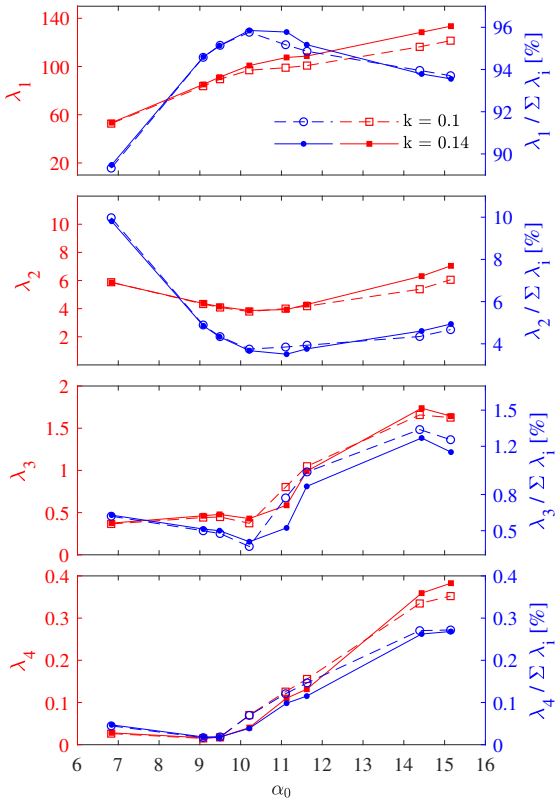

Fig. 11: The eigenvalues and the percentage of their relative contribution to the total modal energy for the first 4 dominant modes across different test cases considered in this study.

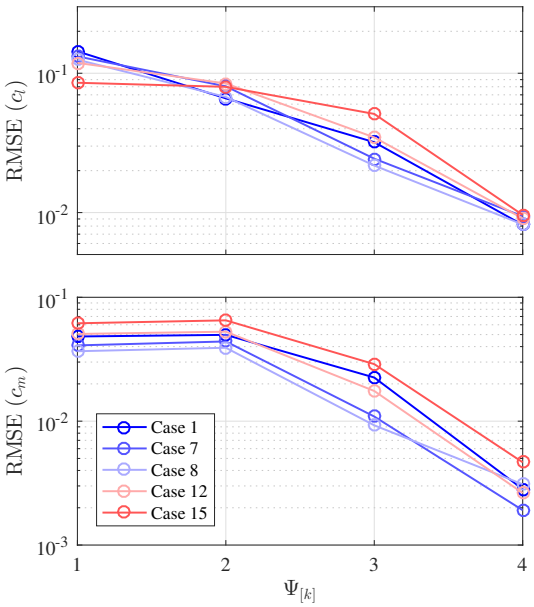

Fig. 12: The RMSE of c_l (top) and c_m (bottom) calculated using reconstructed top and bottom surface pressure distributions. $\Psi_{[k]}$ indicates mode 1 through k are used in c_p reconstructions.

higher suction at the leading edge. As a result, a plateau is observed around stall onset for both absolute and relative values of λ_2, as $a_2(\phi)$ switches sign to hold positive values, followed by a slow growth. It was shown that, as stall progresses in cases with higher α_0 values, the contribution of the third and forth modes become more significant. The eigenvalues for these two modes clearly indicate this behavior as shown in Figure 11. As relative contribution of the first two modes declines for cases with high degree of separation, the eigenvalues for modes 3 and 4 increase indicating higher degrees of contribution toward capturing the pressure distribution during dynamic stall. Another important observation that can be made in this figure is that the eigenvalues for the two different reduced frequencies considered in this study follow the same overall trends across the range of α_0 values studied.

To summarize, examining Figure 11 clearly shows that the cumulative contribution of the first four modes, for any of the cases considered here, captures more than 99.5% of the summed total of all the eigenvalues calculated for that case. This observation confirms the adequacy of the first four global modes in capturing the important features of the surface pressure distribution across a wide range of flow conditions.

4.2.3 Assessing the ability of the modal description in the aerodynamic loads calculation

The ability to calculate aerodynamic loads and moments is extremely important from a practical standpoint. As shown earlier in Figure 7, the reconstructed surface pressure data using only 4 modes can be used for accurate estimation of the aerodynamic loads and moments. To quantitatively assess the accuracy, the error between the experimental load curves and those calculated from modal reconstructions must be evaluated. To represent the accuracy of the calculated loads based on reconstructed surface pressure data, the root-mean-square error (RMSE) is used. It is important to note that the pressure distribution of the bottom surface of the airfoil was also treated similarly for these calculations. A set of global modes are extracted for the bottom surface and then are used in tandem with those from top surface for approximating the loads and moments. The RMSE is calculated using

$$RMSE(c_l) = \sqrt{\frac{\sum_\phi (c_l|_{exp} - c_l|_{\Psi_{[k]}})^2}{N_\phi}}, \tag{5}$$

where the subscript $[k]$ indicates that modes 1 through k have been used for reconstructing the surface pressure data and N_ϕ is the number of bins used to calculate the phase averaged pressure coefficients in a full cycle. A similar approach is used for calculating the $RMSE(c_m)$. Except for the deep stall case (case 15), all cases show a decreasing $RMSE(c_l)$ trend as the number of modes included increases. For the deep stall case, modes 3 and 4 are essential for capturing the features in c_p that significantly affect the aerodynamic loads. This is clear from the rapid decrease in error observed for case 15 as modes 3 and 4 are added. Note that, for the pitching moment, the addition of the second mode does not significantly affect the error of approximation. However, adding modes 3 and 4 significantly reduces the $RMSE(c_m)$ for all cases shown. It is clear that, by considering the first four global modes, both c_l and c_m are well approximated for all the test cases.

5 Summary, conclusions, and future work

In this study, POD was utilized in studying the unsteady pressure distribution on a pitching airfoil. First, phase averaged surface pressure data along with lift and moment coefficients were used to study the airfoil aerodynamics across a wide range of conditions. Analyzing the pressure distributions across cases with different levels of flow separation intensity exhibited clear changes that encouraged modal analysis. Modal analysis was then performed on the unsteady surface pressure data from several different angle-of-attack cases to determine its effectiveness in capturing distinct physical features in the pressure distribution. It was shown that the first four global spatial modes extracted from surface pressure data reflect important and understandable attributes of the c_p distribution for an oscillating airfoil. The results indicate that, while the summation of modes 1 and 2 can accurately capture the attributes of the pressure distribution prior to stall, the addition of modes 3 and 4 is necessary for reconstructing the pressure fluctuations associated with flow separation and reattachment encountered in dynamic stall. These four modes were sufficient to reconstruct the surface pressure data even for a test case with complex unsteady flow interactions. The resulting four-mode reconstructed pressure distributions were used to calculate lift and moment coefficients with good accuracy.

A detailed examination of the modes and their phase-varying coefficients enabled understanding their physical role in reconstructing different attributes of the unsteady surface pressure distribution. The efficacy of four modes in reconstructing the important details of the pressure distribution across a wide range of conditions suggests that low-dimensional representation of unsteady airfoil aerodynamics is feasible. However, to ensure that all important features of the unsteady surface pressure distributions can be captured, it is critical to acquire data in a wide range of conditions as a precursor to data synthesis for effective global mode extraction. Global modes provide a common basis for representing an entire range of dynamic stall cases. This is a key step in enabling the use of POD analysis, as a unique framework, for applications such as CFD validation or flow-state estimation.

Future research should consider a wider range of flow conditions. For example, a wider range of angle of attack schedules in addition to other Reynolds and Mach number regimes can provide valuable insight on the uniqueness of the global modes across complex flow conditions. Future research should also include additional airfoil geometries, in particular thinner airfoils that are known to induce stronger instances of dynamic stall vortex shedding with more complex surface pressure signatures. Simultaneous flow-field measurements would be useful for associating the POD modes extracted from velocity fields to those extracted from surface pressure distributions. Such results can provide significant insight about the dynamics of the energy-containing structures in unsteady flows and their effect on the surface pressure distribution from a low-dimensional perspective. The approach introduced in this work is as applicable to computational results as it is for experimental measurements. This suggests that modal analysis could also serve as an effective means for comparing computation and experiment for validation purposes.

Appendix A

It was mentioned in the Approach section that the POD analysis results in optimal basis functions that can be used to describe a given scalar or vector field. Further discussion regarding the optimal nature of the POD reconstruction is beyond the scope of this work. However, the important takeaway for the purpose of this work is that, for a certain number of modes (less than N), equation 4 will approximate the pressure distribution $c_p(x/c, \phi)$ with the least error compared to any other modal decomposition approach. To find the optimal modes and associated eigenvalues, equation 2 has to be solved. To streamline the adoption of the methodology and analysis for interested reader, formatting the measurements to calculate the correlation matrix is presented here followed by instructions for solving the eigenvalue problem.

Preparation of the data matrix for POD analysis

Similar to other modal analysis techniques, the data matrix for POD analysis has to include a set of column vectors, each containing the spatial distribution of the data at a separate time instance. Here, each column vector contains the phase-averaged values at discrete pressure tap locations along the chord at phase instance ϕ_j that can be written in the following form

$$C_{p_{\phi_j}} = \begin{bmatrix} c_{p_1} \\ c_{p_2} \\ \vdots \\ c_{p_i} \\ \vdots \\ c_{p_n} \end{bmatrix}_{\phi_j} . \tag{6}$$

Here, c_{p_i} represents the phase-averaged pressure coefficient at the ith surface tap location, and n is the number of pressure taps on the airfoil surface. Subsequently, the data matrix F can be formed by stacking the column vectors associated with different phase angles

$$F = [C_{p_{\phi_1}}, ..., C_{p_{\phi_j}}, ..., C_{p_{\phi_{N_\phi}}}], \tag{7}$$

where N_ϕ represents the number of bins in the phase averaging process. Note that, in this work, modes were determined using the data from multiple stall cases altogether. To form the comprehensive data matrix F_C, each set of phase-averaged measurements were stacked one after another to form a long data matrix $F_C = [F_1, F_2, ..., F_g]$, where g is the number of different stall cases used in the analysis. As described by Taylor and Glauser (2004), this approach allows for extracting global POD modes. Also for the purpose of simplification, two separate data matrices are constructed to separate the pressure distribution of the top and bottom surfaces of the airfoil. Once the data matrix is constructed for the airfoil surface under study, the correlation matrix can be calculated using

$$R = \frac{1}{N_\phi \cdot g} F_C {F_C}^T. \tag{8}$$

Solving the eigenvalue problem

To solve the eigenvalue problem and determine the POD modes, one can take advantage of the robustness of the Singular Value Decomposition (SVD) (Tu et al., 2013; Taira et al., 2017). Since the correlation matrix R is symmetric, then SVD takes into account the symmetry of R such that

$$R = U \Lambda U^T. \tag{9}$$

Since R is real, the matrix U is a real orthogonal matrix whose columns are the eigenvectors Ψ_k of R and Λ is a real and diagonal matrix that contains the corresponding eigenvalues λ_k of R. For further information regarding equation 9 see Ikramov (2012).

Appendix B

Due to the large amount of spatial and temporal pressure data associated with a pitching airfoil, it is difficult to graphically portray the evolution of the pressure distribution over time and space for a full pitching cycle. To address this issue, phase-averaged c_p contours are used throughout this paper. This Appendix provides a detailed description of such contour representation to help the reader with the interpretation of the data.

A deep dynamic stall case is selected to highlight the features in the phase-averaged pressure distribution over the top and bottom surfaces of the airfoil. The c_p distributions for the top and bottom surfaces of the airfoil are denoted by Figure 13 (a) and (b) respectively. The pressure coefficients are presented as a function of relative chord position x/c and phase of the the pitch cycle ϕ. The colors represent the values of the pressure coefficients for a particular x/c and ϕ as indicated by the color bar. For reference, the angle of attack α is included on the right vertical axis. The initial point in the cycle $\phi = 0$ corresponds to the minimum α at the beginning of the rising phase (denoted by R), proceeds to the maximum α at $\phi = \pi$, and then returns back to the minimum α again at $\phi = 2\pi$ at the end of the falling phase (denoted by F). In this particular case, the minimum α is 9.5°, and the maximum α is 20.9°. This

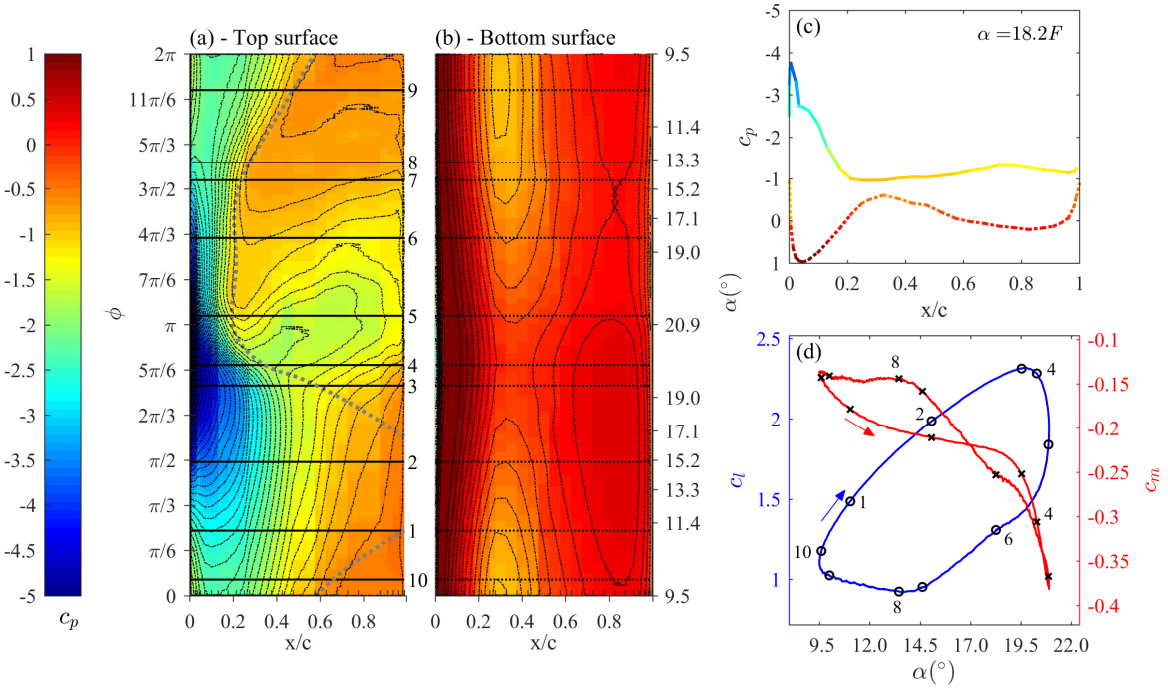

Fig. 13: Pressure distributions and integrated loads for $\alpha = 15.2^\circ \pm 5.7^\circ$ & $k = 0.14$. Phase-averaged pressure coefficients (c_p) plotted against airfoil x/c location, point in the motion phase ϕ, and angle of attack α for (a) the suction and (b) pressure surfaces of the airfoil. The gray dotted line overlaid on the pressure distributions of the top surface separates the attached and separated flow regions. Conventional representation of the pressure coefficient distribution (c) at $\alpha = 18.2^\circ$ *falling* is shown to help the reader with the interpretation of the contour representation. Lift and moment coefficients (d) are shown as a function of angle of attack, where the numbers correspond to the lines in (a) and (b).

style of presenting the surface pressure distribution allows for a large amount of pressure information (for an entire cycle) to be visualized in a single figure. For instance, examine the traditional pressure coefficient plots shown in Figure 13 (c). This figure represents the pressure distribution at $\alpha = 18.2^\circ$ in the falling phase of the airfoil motion. The dark blue color indicates the suction peak on the leading edge of the airfoil. The nearly constant value of the pressure distribution near the trailing edge corresponds to a separated condition on the top surface of the airfoil at this angle of attack. Lift and moment coefficients are also shown in Figure 13 (d) as a function of α to highlight the coupling between the c_p distribution and aerodynamic loading derived from the pressure distribution. A set of number-designated lines and markers are used on the pressure contours and the load curves to highlight the important incidents that take place in the cycle.

The pressure distributions are further examined to consider what can be learned from such representation of unsteady pressure data and how different flow features associated with dynamic stall are revealed by the c_p distribution. At $\alpha = 11^\circ R$ (point 1), the continuous change in the pressure distribution along the chord near the trailing edge indicates attached flow on the top side of the airfoil. As airfoil's rising motion continues, the suction peak near the leading edge increases, and lift continues to increase beyond the static stall angle ($\alpha_{ss} = 12^\circ$). Note that, due to the cusp in the airfoil lower surface near the trailing edge (see Figure 2), the nose-down pitching moment c_m is significantly affected by the flow on the pressure side. As shown in Figure 13 (b), the increase of the pressure on the trailing edge and consequent change in the location of the center of pressure results in a continuous decrease of c_m values even at lower angles of attack, between points 1 and 3, where the pressure distribution indicates that the flow is attached on the top surface. As airfoil passes $\alpha = 15.2^\circ R$ (point 2) and approaches $19.1^\circ R$ (point 3), the iso-c_p contour lines in Figure 13(a) start to turn in the chord-wise direction. For unsteady airfoils, the intensifying adverse pressure gradient imposed by the geometry and airfoil's increasing incidence generally induces a thin layer of recirculating flow on the top surface near the trailing edge. This process reduces the gradient of the pressure distribution near the trailing edge that is observed here between points 2 and 3. This process is commonly referred to as viscous decambering (Gross, 1979; Drela, 2014). Note that, between points 2 and 3, the increase in the magnitude of the suction peak maintains the growth of the c_l (with slower rate). But, at the same time, changes in the pressure distribution over the trailing edge initiate the c_m stall, the rapid decrease in moment observed just before point 3. Maximum c_l occurs

at $\alpha = 19.5^\circ R$ followed by a plateau as the suction peak reaches its maximum value (point 3). A rounded peak in the c_l curve is observed that is associated with the thick and rounded leading-edge geometry of the airfoil under study (Winslow et al., 2018). Beyond $\alpha = 19.5^\circ R$ (point 3), the high suction region on the front part of the airfoil shrinks significantly indicating the occurrence of flow separation. As airfoil approaches the maximum angle of attack, the highly adverse pressure gradient and the slow-down of the airfoil pitch-up motion (see the description of the pitch rate-induced flow acceleration effect by Ericsson and Reding (1971)) significantly decrease the momentum of the shear layer that eventually results in flow separation. The rise in the suction felt on the trailing edge of the airfoil that can be observed in Figure 13(a) between points 4 and 6 is consistent with the formation and convection of unsteady vortical structures induced during the detachment of the shear layer (McCroskey et al., 1976). However, the pressure distribution indicates a slower and weaker dynamic stall vortex detachment process compared to that of a thinner airfoil undergoing leading-edge stall. Note that, for the thick and rounded leading-edge geometry of the airfoil under study, the flow remains attached on the leading edge throughout the entire cycle, as indicated by the high suction region and lack of rapid bursting of a strong leading-edge vortex (McCroskey et al., 1976; Amandolèse and Széchényi, 2004). For a detailed discussion of dynamic stall phenomenon, the reader is encouraged to consult the literature (Lipinski et al., 2008; Mulleners and Raffel, 2012; Eldredge and Jones, 2019). For the remainder of the falling phase, the pressure distribution over the top surface indicates that the flow remains separated over much of the airfoil. At the end of the falling phase, a chord-wise expansion of the suction beyond $\alpha = 13.3^\circ F$ (point 8) indicates the beginning of the reattachment process from leading edge that continues for the rest of the falling phase into the next cycle. The reattachment process ends during the rising phase of the next cycle.

Acknowledgements The authors wish to thank J. Strike, M. Hind, A. Magstadt, and T. Harms for their assistance during the wind tunnel measurements and data analysis. In addition, the first author gratefully acknowledges the financial support from the College of Engineering and Applied Science under the University of Wyoming's Tier-1 Engineering Initiative.

Declarations

Ethical Approval

Not Applicable

Competing interests

Not Applicable

Authors' contributions

Pourya Nikoueeyan determined content and organization of the paper, wrote the main manuscript and prepared the figures. He also reviewed the document. Jonathan Naughton determined the content and organization of the of paper and edited the paper.

Funding

Funding for this work was received from the College of Engineering and Applied Science under the University of Wyoming's Tier-1 Engineering Initiative.

Availability of data and materials

Data is available from the authors upon request.

References

Alfonsi, G., Primavera, L., Passoni, G. and Restano, C. (2001). Proper orthogonal decomposition of turbulent channel flow, *Computational Fluid Dynamics 2000*, Springer Berlin Heidelberg, pp. 473–478.

Ali, M., Pandey, A. and Gregory, J. (2016). Dynamic mode decomposition of fast pressure sensitive paint data, *Sensors* **16**(6): 862.

Amandolèse, X. and Széchényi, E. (2004). Experimental study of the effect of turbulence on a section model blade oscillating in stall, *Wind Energy* **7**(4).

Bakewell, H. P. and Lumley, J. L. (1967). Viscous sublayer and adjacent wall region in turbulent pipe flow, *Physics of Fluids* **10**(9): 1880–1889.

Barone, M. F., Berg, D. E., Devenport, W. J. and Burdisso, R. (2009). Aerodynamic and aeroacoustic tests of a flatback version of the DU97-W-300 airfoil, *Technical Report SAND2009-4185*, Sandia National Laboratories.

Buljak, V. (2012). *Inverse Analyses with Model Reduction*, 1 edn, Springer-Verlag Berlin Heidelberg.

Carr, L. W. (1988). Progress in analysis and prediction of dynamic stall, *Journal of Aircraft* **25**(1): 6–17.

Cazemier, W., Verstappen, R. W. C. P. and Veldman, A. E. P. (1998). Proper orthogonal decomposition and low-dimensional models for driven cavity flows, *Physics of Fluids* **10**(7): 1685–1699.

Citriniti, J. H. and George, W. K. (2000). Reconstruction of the global velocity field in the axisymmetric mixing layer utilizing the proper orthogonal decomposition, *Journal of Fluid Mechanics* **418**: 137–166.

Coleman, D. G., Thomas, F. O., Gordeyev, S. and Corke, T. C. (2019). Parametric modal decomposition of dynamic stall, *AIAA Journal* **57**(1): 176–190.

Davidson, P., Naughton, J. and Sitaraman, J. (2015). Modern testing approaches used to characterize dynamic stall regimes on helicopter airfoils, *71th AHS International's Annual Forum*, American Helicopter Society International.

Drela, M. (2014). *Flight vehicle aerodynamics*, MIT Press.

Dunne, R. and McKeon, B. J. (2015). Dynamic stall on a pitching and surging airfoil, *Experiments in Fluids* **56**(8).

Durgesh, V. and Naughton, J. W. (2010). Multi-time-delay LSE-POD complementary approach applied to unsteady high-Reynolds-number near wake flow, *Experiments in Fluids* **49**(3): 571–583.

Eldredge, J. D. and Jones, A. R. (2019). Leading-edge vortices: Mechanics and modeling, *Annual Review of Fluid Mechanics* **51**(1): 75–104.

Ericsson, L. E. and Reding, J. P. (1971). Unsteady airfoil stall, review and extension, *Journal of Aircraft* **8**(8): 609–616.

Ericsson, L. and Reding, J. (1988). Fluid mechanics of dynamic stall part i. unsteady flow concepts, *Journal of Fluids and Structures* **2**(1): 1–33.

George, W. K. (1988). Insight into the dynamics of coherent structures from a proper orthogonal decomposition, *International Seminar on Wall Turbulence*.

Glauser, M. N., Young, M. J., Higuchi, H., Tinney, C. E. and Carlson, H. (2004). POD based experimental flow control on a NACA-4412 airfoil (invited), *42nd AIAA Aerospace Sciences Meeting and Exhibit*, American Institute of Aeronautics and Astronautics.

Gordeyev, S., Lucca, N. D., Jumper, E. J., Hird, K., Juliano, T. J., Gregory, J. W., Thordahl, J. and Wittich, D. J. (2014). Comparison of unsteady pressure fields on turrets with different surface features using pressure-sensitive paint, *Experiments in Fluids* **55**(1).

Gordeyev, S. V. and Thomas, F. O. (2013). A Temporal Proper Decomposition (TPOD) for closed-loop flow control, *Experiments in Fluids* **54**(3): 1477.

Gross, L. W. (1979). Multi-element airfoil viscous-inviscid interactions, *Technical Report NASA-CR-159125*, National Aeronautics and Space Administration.

Harms, T., Nikoueeyan, P. and Naughton, J. W. (2018). Modal analysis of the cycle-to-cycle variations observed in dynamic stall, *74th Annual Forum and Technology Display*, American Helicopter Society International.

Hind, M. D., Nikoueeyan, P. and Naughton, J. W. (2017). Quantification of uncertainty in the correction of remotely measured unsteady pressure signals on pitching airfoils, *33rd AIAA Aerodynamic Measurement Technology and Ground Testing Conference*, American Institute of Aeronautics and Astronautics.

Holmes, P., Lumley, J. L., Berkooz, G. and Rowley, C. W. (2012). *Turbulence, Coherent Structures, Dynamical Systems and Symmetry*, Cambridge Monographs on Mechanics, 2 edn, Cambridge University Press.

Ikramov, K. D. (2012). Takagi's decomposition of a symmetric unitary matrix as a finite algorithm, *Computational Mathematics and Mathematical Physics* **52**(1): 1–3.

Kopp, G. A., Ferre, J. A. and Giralt, F. (1997). The use of pattern recognition and proper orthogonal decomposition in identifying the structure of fully-developed free turbulence, *Journal of Fluids Engineering* **119**(2): 289–296.

Lee, T. and Gerontakos, P. (2004). Investigation of flow over an oscillating airfoil, *Journal of Fluid Mechanics* **512**.

Leishman, J. G. (2002). *Principles of Helicopter Aerodynamics*, Cambridge Aerospace Series, Cambridge University Press.

Lind, A. H. and Jones, A. R. (2016). Unsteady aerodynamics of reverse flow dynamic stall on an oscillating blade section, *Physics of Fluids* **28**(7): 077102.

Lipinski, D., Cardwell, B. and Mohseni, K. (2008). A lagrangian analysis of a two-dimensional airfoil with vortex shedding, *Journal of Physics A: Mathematical and Theoretical* **41**(34): 344011.

Lumley, J. L. (1967). The structure of inhomogeneous turbulent flows, *in* A. M. Yaglam and V. I. Tatarsky (eds), *Proceedings of the International Colloquium on the Fine Scale Structure of the Atmosphere and Its Influence on Radio Wave Propagation*, Doklady Akademii Nauk SSSR, Nauka, Moscow.

Macdonald, P., Holmes, J. and Kwok, K. (1990). Wind loads on circular storage bins, silos and tanks III. fluctuating and peak pressure distributions, *Journal of Wind Engineering and Industrial Aerodynamics* **34**(3): 319–337.

Mariappan, S., Gardner, A. D., Richter, K. and Raffel, M. (2014). Analysis of dynamic stall using dynamic mode decomposition technique, *AIAA Journal* **52**(11): 2427–2439.

McAlister, K. W., Carr, L. W. and McCroskey, W. J. (1978). Dynamic stall experiments on the NACA 0012 airfoil, *Technical Report 19780009057*, National Aeronautics and Space Administration.

McCroskey, W., Carr, L. and McAlister, K. (1976). Dynamic stall experiments on oscillating airfoils, *AIAA Journal* **14**(1).

McCroskey, W. J. (1977). The 1976 freeman scholar lecture: Some current research in unsteady fluid dynamics, *Journal of Fluids Engineering* **99**(1).

McCroskey, W. J. (1981). The phenomenon of dynamic stall, *Technical report*, National Aeronautics and Space Administration.

Melius, M., Cal, R. B. and Mulleners, K. (2016). Dynamic stall of an experimental wind turbine blade, *Physics of Fluids* **28**(3): 034103.

Mulleners, K. and Raffel, M. (2012). The onset of dynamic stall revisited, *Experiments in Fluids* **52**(3): 779–793.

Mulleners, K. and Raffel, M. (2013). Dynamic stall development, *Experiments in Fluids* **54**(2).

Naughton, J. W., Strike, J. A., Hind, M. D., Magstadt, A. A. and Babbitt, A. (2013). Measurement of dynamic stall on the DU wind turbine airfoil series, *69th AHS International's Annual Forum*, American Helicopter Society International.

Nikoueeyan, P., Hind, M. D., Strike, J., Singh, M., Naughton, J. W., Keeter, S. and Dahland, M. (2019). Characterization of unsteady pressures on a blunt trailing edge using a direct-mount pressure scanner, *AIAA Aerospace Sciences Meeting*, A, American Institute of Aeronautics and Astronautics.

Nikoueeyan, P., Strike, J., Magstadt, A., Hind, M. and Naughton, J. W. (2014). Characterization of the aerodynamic coefficients of a wind turbine airfoil with a Gurney flap for flow control applications, *32nd AIAA Applied Aerodynamics Conference*, American Institute of Aeronautics and Astronautics.

Ramasamy, M., Wilson, J. S., McCroskey, W. J. and Martin, P. B. (2018). Characterizing cycle-to-cycle variations in dynamic stall measurements, *Journal of the American Helicopter Society* **63**(2): 1–24.

Rowley, C. W. and Dawson, S. T. (2017). Model reduction for flow analysis and control, *Annual Review of Fluid Mechanics* **49**(1): 387–417.

Seidel, J., Siegel, S., Cohen, K. and McLaughlin, T. (2005). POD based separation control on the NACA0015 airfoil, *43rd AIAA Aerospace Sciences Meeting and Exhibit*, American Institute of Aeronautics and Astronautics.

Strike, J. A., Hind, M. D., Saini, M. S., Naughton, J. W., Wilson, M. D. and Whitmore, S. A. (2010). Unsteady surface pressure reconstruction on an osculating airfoil using the Wiener deconvolution method, *27th AIAA Aerodynamic Measurement Technology and Ground Testing Conference*, number 2010-4799, American Institute of Aeronautics and Astronautics.

Taira, K., Brunton, S. L., Dawson, S. T. M., Rowley, C. W., Colonius, T., McKeon, B. J., Schmidt, O. T., Gordeyev, S., Theofilis, V. and Ukeiley, L. S. (2017). Modal analysis of fluid flows: An overview, *AIAA Journal* **55**(12): 4013–4041.

Taira, K., Hemati, M. S., Brunton, S. L., Sun, Y., Duraisamy, K., Bagheri, S., Dawson, S. T. M. and Yeh, C.-A. (2019). Modal analysis of fluid flows: Applications and outlook, *AIAA Journal* pp. 1–25.

Tamura, Y., Suganuma, S., Kikuchi, H. and Hibi, K. (1999). Proper orthogonal decomposition of random wind pressure field, *Journal of Fluids and Structures* **13**(7-8): 1069–1095.

Taylor, J. A. and Glauser, M. N. (2004). Towards practical flow sensing and control via POD and LSE based low-dimensional tools, *Journal of Fluids Engineering* **126**(3): 337–345.

Tu, J. H., Griffin, J., Hart, A., Rowley, C. W., Cattafesta, L. N. and Ukeiley, L. S. (2013). Integration of non-time-resolved PIV and time-resolved velocity point sensors for dynamic estimation of velocity fields, *Experiments in Fluids* **54**(2): 1429.

Walton, S., Hassan, O. and Morgan, K. (2013). Reduced order modelling for unsteady fluid flow using proper orthogonal decomposition and radial basis functions, *Applied Mathematical Modelling* **37**(20): 8930 – 8945.

Whitmore, S. A. and Wilson, M. D. (2011). Wiener deconvolution for reconstruction of pneumatically attenuated pressure signals, *AIAA* **49**: 890–897.

Widmann, A. and Tropea, C. (2017). Reynolds number influence on the formation of vortical structures on a pitching flat plate, *Interface Focus* **7**(1): 20160079.

Winslow, J., Otsuka, H., Govindarajan, B. and Chopra, I. (2018). Basic understanding of airfoil characteristics at low reynolds numbers ($10^4 - 10^5$), *Journal of Aircraft* **55**(3): 1050–1061.